Journal of Hazardous Materials 487 (2025) 137203

Contents lists available at ScienceDirect

Journal of Hazardous Materials

journal homepage: www.elsevier.com/locate/jhazmat

Tuning multi-scale pore structures in carbonaceous films via direct ink writing and sacrificial templates for efficient indoor formaldehyde removal

Zhuo Chen [b], Qiwei Chen [c,d], Yan Wang [d], Wuwei Zou [d], Yuan Li [b], Jinhan Mo [a,d,e,f,g,*]

[a] Key Laboratory of Coastal Urban Resilient Infrastructures (Ministry of Education), College of Civil and Transportation Engineering, Shenzhen University, Shenzhen 518060, China
[b] Department of Civil and Environmental Engineering, The Hong Kong Polytechnic University, Kowloon, Hong Kong
[c] China Construction First Group Construction & Development Co., Ltd., Beijing 100102, China
[d] Beijing Key Laboratory of Indoor Air Quality Evaluation and Control, Department of Building Science, Tsinghua University, Beijing 100084, China
[e] State Key Laboratory of Intelligent Geotechnics and Tunnelling, Shenzhen University, Shenzhen 518060, China
[f] State Key Laboratory of Subtropical Building and Urban Science, Shenzhen 518060, China
[g] Key Laboratory of Eco Planning & Green Building (Tsinghua University), Ministry of Education, Beijing 100084, China

HIGHLIGHTS

- Dimensionless $A^*{\cdot}St_m$ and Di^* were proposed to optimize film VOC adsorption.
- Multi-scale porous films were made by the DIW printing and sacrificial template.
- Efficient and long-term formaldehyde removal was achieved by the developed film.
- The film EAC_{ad} and energy cost outperformed literature and commercial products.

GRAPHICAL ABSTRACT

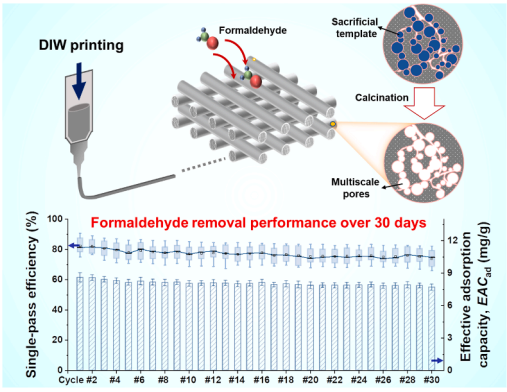

ARTICLE INFO

Keywords:
Direct ink writing
Adsorption
Formaldehyde
Multiscale pore structure
Mass transfer kinetics

ABSTRACT

The primary challenges impeding the extensive application of adsorption for indoor air purification have been low efficiency and effective capacity. To fill the research gap, we developed carbonaceous net-like adsorption films featuring multi-scale porous structures for efficient indoor formaldehyde removal. By optimizing the interfacial mass transfer and internal diffusion, we designed macro- to mesoscale meshes on the film surface and micro- to nano-scale pores within the materials, which were achieved by direct-ink-writing (DIW) printing and sacrificial template methods, respectively. Compared to unmodified planar films, the developed films exhibited a significant increase in the initial single-pass efficiency of formaldehyde from 68.1 % to 89.0 %, with the 8-hour effective adsorption capacity (EAC_{ad}) spiking from 2.74 mg/g to 8.60 mg/g. Through thermal regeneration, the film demonstrated stable operation for 30 days through a long-term experiment over 250 hours, and EAC_{ad}

* Corresponding author at: Key Laboratory of Coastal Urban Resilient Infrastructures (Ministry of Education), College of Civil and Transportation Engineering, Shenzhen University, Shenzhen 518060, China.
E-mail address: mojinhan@szu.edu.cn (J. Mo).

https://doi.org/10.1016/j.jhazmat.2025.137203
Received 21 October 2024; Received in revised form 29 November 2024; Accepted 12 January 2025
Available online 15 January 2025

significantly increased to 241.7 mg/g. The multi-scale adsorption films achieved nearly the highest purification rates and capacities among existing physisorption and chemisorption technologies, with the lowest energy cost of 0.37 kW·h per day. The innovative design and fabrication of multi-scale adsorption films evidence its substantial application for indoor formaldehyde purification and provide a viable solution for carbon capture and gas separation in environmental engineering.

1. Introduction

In recent years, the issue of indoor environmental pollution, including aerosols [1–3] and organic pollutants [4–6], has garnered significant attention due to its detrimental impact on human health and contribution to substantial economic losses. Volatile organic compounds (VOC), a category of organic pollutants, are particularly concerning, with estimated costs of disease burden exceeding 100 billion CNY in 2017 [7,8]. Persistent emissions from furniture and coatings lead to ongoing VOC pollution within indoor environments [9,10], the purification of which results in huge building energy consumption [11]. The chronic toxicity associated with VOC pollution has been widely reported, linked to an increased risk of severe diseases [12–16], with formaldehyde classified as a Class 1 carcinogen by the World Health Organization.

Adsorption is a widely recognized and effective technique for removing indoor organic pollutants [17,18]. When designed optimally, adsorption components can efficiently remove low-concentration VOCs [19,20]. Strategies to enhance adsorption performance include ensuring adequate contact between the adsorbent and pollutants, optimizing mass transfer kinetics, and reducing airflow resistance [21–23]. Structured monolithic adsorption devices have attracted increasing research interest due to their channel structures [24,25], which facilitate effective contact between VOCs and adsorbents while minimizing airflow pressure drop [26,27]. The critical components of these devices are the adsorption films, which contain highly efficient VOC adsorbents and have been the subject of extensive research [28,29].

Conventionally, adsorption films are fabricated by coating a slurry of adsorption material onto an electrothermal substrate, followed by a drying process [29]. However, this method has several limitations, including extended preparation time, increased labor costs, and non-uniformity in the adsorption coating, as well as challenges in achieving uniform films with intricate interfacial structures. Electrospinning is another effective technique to prepare polymer fiber membranes and adsorption layers with multi-level porous carbon structures [30], the products of which were widely applied for pollutant adsorption [31], desulfurization [32] and water treatment [33]. Nevertheless, the application of electrospinning might be hindered by a series of problems, including strict requirements on preparation condition precisions and source materials for the adsorption layer [34]. Thus, a simple and efficient technology is urgently required for adsorption-film preparation.

To overcome the above-mentioned limitations, direct ink writing (DIW) has been utilized for the preparation of adsorption films [35–38]. The semi-liquid adsorbent ink, characterized by high solid loading ratios and shear-thinning rheological properties, retains its shape post-printing [39,40]. The flexibility and versatility of DIW facilitate the automated fabrication of adsorption components with enhanced mass transfer kinetics [41]. Despite the advantages of DIW, a challenge impedes its widespread application: the diffusion of VOCs through the intrinsic nanopores into the carbon material of DIW-fabricated film remains slow [42]. Researchers have tried to fabricate more microsized pores and interconnected hierarchical porous structures in adsorbents to accelerate the inward diffusion rate [43]. Nevertheless, the resolution limitations of DIW hinder the achievement of submicron-micron-sized structures in adsorption films, hindering the achievement of good VOC-diffusional performance.

Recently, starch has been explored as a precursor material for DIW printing and subsequently carbonized to prepare an adsorption film for further application in indoor air purification. The advantages of starch used for DIW printing can be classified as three points: 1) starch can be artificially synthesized, thus resulting in a wide and low-cost source [44]; 2) the main product obtained after the carbonization of starch is activated carbon, which has the ability to provide multiple adsorption sites for air purification [45–47]; 3) starch will undergo gelatinization and amorphous transformation at specific high temperatures, and then facilitate further material processing [29]. Crucially, in an amorphous ink, the inclusion of template particles at microscales can create submicron-sized pore structures, potentially enhancing VOC diffusion in DIW-fabricated films [48]. Thus, employing starch as a precursor in DIW inks for activated-carbon adsorbent materials presents a significant opportunity to prepare submicron-scale pore structures within the material.

In this study, we fabricated a net-like adsorption film featuring multiscale porous structures through a combination of DIW and sacrificial templating techniques. Starch was selected as the adsorbent precursor to achieve pore induction via sacrificial templates. Polymethylmethacrylate (PMMA) served as the sacrificial template to generate controllable nano- to micron-sized pores, thereby enhancing the inward diffusion rate of VOCs within the adsorption film. Formaldehyde was chosen as the target VOC for purification experiments. Experiments were conducted to validate the adsorption capabilities of the multiscale porous adsorption film.

2. Mathematical analysis of mass transfer

2.1. Mass transfer analysis and optimization principle of adsorption film

The mass transfer process and modeling schematic of VOCs from the gas phase to the adsorption film inside the indoor VOC adsorption module are illustrated in Fig. 1(a) and (b). There are two widely applied assumptions used in the mass transfer model of this study: 1) we assumed a one-dimensional flow for the airflow dynamics [49,50]. It means that the gaseous VOC concentration is considered to change only with the flow direction in the air duct, and is evenly distributed on the cross-section of flow; 2) the VOC pollutant is assumed to follow the partition theory at the gas-solid interface of the adsorbent material [51]. We then established the coordinate system in Fig. 1(b), with the z coordinate representing the airflow direction and the x coordinate for the VOC diffusion direction inside the adsorption film. The VOC mass transfer process in the differential unit, marked as the box with red color in Fig. 1(b), can be modeled as a one-dimensional partial differential equation based on the assumptions, as shown in Eqs. (1) and (2). Details about the derivation process are summarized in Supplementary *Section S1*.

$$\frac{\partial C(z)}{\partial t} = -\frac{G}{H \cdot L_s}\frac{\partial C(z)}{\partial z} - \frac{r(z)}{H} \tag{1}$$

$$r(z) = h_m\left[C(z) - C_s(x,z)|_{x=0}\right] = D_e K \left.\frac{\partial C_s(x,z)}{\partial x}\right|_{x=0} \tag{2}$$

where, z is the coordinate along the airflow direction; H and L_s are the height and width of the air duct perpendicular to the direction of airflow, respectively, m; $C(z)$ is the VOC concentration that varies over time (t, s) and airflow direction (z coordinate), mg/m^3, which, specifically, valued as inlet concentration C_{in} at the $z = 0$ position; G stands for

the airflow rate, m^3/s; $r(z)$ is the adsorption rate per unit area, mg/(m^2•s); h_m is the mass-transfer coefficient of VOCs on adsorption film, m/s; $C_s(x, z)$ is the gaseous VOC concentration adjacent to the solid structure inside the adsorption film, mg/m^3, varied over time, airflow direction (z coordinate) and thickness direction (x coordinate); while $C_s(x,z)|_{x=0}$ stands for the $C_s(x, z)$ at the interface adjacent to the top of the adsorption film, which is abbreviated as $C_{s,top}(z)$ in the following sections; D_e (m^2/s) is the equivalent diffusion coefficient of VOCs in the material, and K (unitless) is the partition coefficient. Based on Eq. (2), the adsorption rate is proportional to the concentration difference at the gas-solid interface and the first-order concentration differential within the sorption material, indicating the adsorption kinetics of this process can be regarded as the Pseudo-first-order model [52].

Over a short period, the VOC adsorption rate remains stable, resulting in a steady-state mass transfer process. The steady-state mass transfer model can then be derived from Eq. (1) and shown in Eq. (3).

$$G\frac{dC(z)}{dz} = -r(z)L_s \tag{3}$$

Meanwhile, the adsorption rate $r(z)$ can be expressed in terms of $C(z)$ and $C_{s,top}(z)$ based on Eq. (2). The specific equation is provided as Eq. (4), with the deviation detailed in Supplementary *Section S1*.

$$r(z) = \frac{C(z)}{1/h_m + C_{s,top}(z)/\left(D_e K \partial C_{s,top}(z)/\partial x\right)} \tag{4}$$

Combining Eqs. (3) and (4), the solution for $C(z)$ can be obtained as shown below.

$$C(z) = C_{in}\exp\left(-\frac{L_s h_m}{G}\int \frac{1}{1 + h_m C_{s,top}(z)/\left(D_e K \partial C_{s,top}(z)/\partial x\right)}dz\right) \tag{5}$$

Applying the solution of $C(z)$ presented in Eq. (5), the expression for single-pass efficiency (ε), obtained through integrating, is as Eqs. (6) and (7).

$$\varepsilon = \frac{C_{in} - C_{out}}{C_{in}} = 1 - \exp(-NTU_m) \tag{6}$$

$$NTU_m = \frac{h_m A_D}{G}, A_D = L_s \int \left| \frac{1}{1 + h_m C_{s,top}(z)/\left(D_e K \partial C_{s,top}(z)/\partial x\right)} \right|_{z=L_{ad}} \tag{7}$$

where, L_{ad} is the length of the air duct, m. Interestingly, the NTU_m parameter is similar in form to the classic parameter NTU in the field of heat transfer [53], defined as Eq. (8).

$$NTU = \frac{UA}{C_{min}} \tag{8}$$

where, U is the overall heat transfer coefficient of the target heat exchanger, W/m^2·K; A is the effective heat transfer area, m^2; C_{min} represents the minimum thermal capacity rate of the two fluids in the heat exchanger, W/K. The NTU parameter is commonly used to evaluate and optimize the performance of heat exchangers. Generally, a larger NTU indicates better heat-transfer performance. By analogy between heat and mass transfer, the NTU_m parameter characterizes the interface mass-transfer enhancement of pore structures on micro, meso, and macro scale, governed by flow fields, properties of sorption materials, and concentration gradients. The NTU_m parameter can be further non-dimensionalized as the product of three dimensionless parameters, detailed in Eq. (9).

$$NTU_m = A^* St_m Di^* = \frac{A_{sur}}{A_c}\frac{h_m}{u_a}\int \frac{\left| \frac{1}{1+h_m C_{s,top}(z)/\left(D_e K \partial C_{s,top}(z)/\partial x\right)} \right|_{z=L_{ad}}}{L_{ad}} \tag{9}$$

where, A_{sur} is the surface area of adsorption film, m^2, and A_c (equal to $H \times L_s$) represents the cross-sectional area of the air duct, m^2. In Eq. (9), The first two dimensionless terms, A^* and St_m, reflect the influence of gas-solid contact area and the strength of external mass transfer on the adsorption mass transfer process, similar to the formula of

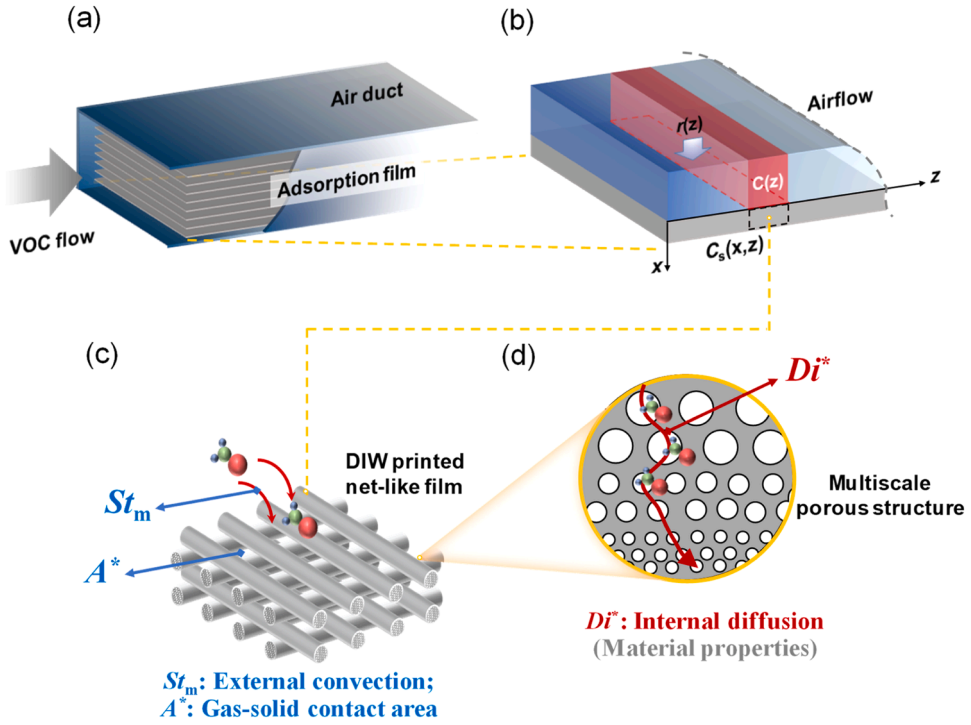

Fig. 1. (a) Schematic diagram of the indoor VOC adsorption component; (b) The mass transfer process of VOCs flowing over the adsorption film in the air duct; (c) schematic of the macrostructure of DIW-printed adsorption film; (d) the mass-transfer diagram of VOCs inside microscopic pore structures of solid materials within the adsorption film.

photocatalysis. Specifically, the St_m parameter is well known as the Stanton number of mass transfer [49]. The physical processes dominated by A^* and St_m can also be seen intuitively in Fig. 1(c). The third term Di^* represents the strength of internal diffusion, which has the most significant influence on the entire process of adsorption mass transfer in porous media (see Fig. 1(d) for details). Considering the expression of Di^* is relatively complex, a simplification was applied to the parameter as Eqs. (10)-(13).

$$Di^* = \frac{\int \frac{1}{1+D_{af}^*} dz \Big|_{z=L_{ad}}}{L_{ad}} \tag{10}$$

$$D_{af}^* = \frac{h_m C_{s,top}}{D_e K \partial C_{s,top}/\partial x} = \frac{Bi_m}{K} \frac{1}{\partial C_{s,top}^*/\partial X} \tag{11}$$

$$Bi_m = \frac{h_m \cdot \delta}{D_e} \tag{12}$$

$$\partial C_{s,top}^*/\partial X = \frac{\partial C_{s,top}/C_{s,top}}{\partial x/\delta} \tag{13}$$

where, Bi_m is the mass transfer Biot number; Bi_m/K represents the ratio of internal mass transfer resistance to interfacial mass transfer resistance in the adsorption process within porous media [54]. This ratio is also known as the dimensionless Little number (*Li*) [55]; $\partial C_s^*/\partial X$ is the dimensionless concentration gradient at the gas-solid interface. These two dimensionless parameters are defined in Eqs. (12) and (13), where δ is the thickness of the adsorption film and the depth of diffusion mass transfer. According to Eq. (9), D_{af}^* can be written as Bi_m/K times the inverse of the dimensionless concentration gradient $\partial C_s^*/\partial X$. In other words, D_{af}^* characterizes the speed of diffusion within the material by representing the ratio of internal mass transfer resistance to interfacial mass transfer resistance multiplied by the inverse of the concentration gradient.

The adsorption behaviors of VOCs are expected to be improved through pathways that result in a larger NTU_m. As the dimensionless parameters (A^*, St_m and Di^*) dominating NTU_m can be divided into two categories: the product of A^* and St_m ($A^* \cdot St_m$) reflecting the gas-solid interfacial mass transfer intensity during adsorption, and Di^* indicating the internal diffusion mass transfer during purification. Based on this analysis, this study proposes the following structural optimization ideas for the adsorption film:

(1) **Construct mesh structures at macro- and meso-scales on the film surface to enlarge the $A^* \cdot St_m$ parameter.** This involves creating millimeter- to micrometer-scale structures at the material interface to increase the gas-solid contact area and enhance external convection, thereby increasing the gas-solid interfacial mass transfer flux. The net-like structures on surfaces can enlarge the contact area, thereby increasing the interfacial mass transfer area A^*. Convective mass transfer at the interface will also be enhanced, resulting in a larger h_m as well as St_m.

(2) **Generate micro- to nano-scale pores inside the sorption materials to increase the Di^* parameter.** According to Eqs. (10)-(13), Di* is determined by the dimensionless parameters Bi_m/K (characterizing the ratio of internal to external mass transfer resistance) and the dimensionless concentration gradient $\partial C_{s,top}/\partial X$. The generation of micro- to nano-scale pores can adjust the pore rate and tortuosity inside the sorption materials, which will enhance diffusion mass transfer and reduce internal resistance. This results in the decrease of Bi_m/K, thereby increasing Di^*. Meanwhile, enhancing internal diffusion can effectively weaken the accumulation of interface concentration, attenuating the decrease in the concentration gradient $\partial C_{s,top}/\partial X$.

2.2. Evaluation method for adsorption efficiency improvement

According to the above theoretical derivation, the structural performance improvement for the adsorption film can be attributed to the dimensionless interfacial mass transfer parameter $A^* \bullet St_m$ and the internal diffusion parameter Di^*. We developed an evaluation method to analyze the adsorption efficiency improvement. As shown in Eq. (14), the NTU_m before and after the performance enhancement is compared. By taking the logarithm of both sides of the equation, Eq. (15) is obtained. The equation is then normalized and multiplied by $\Delta\varepsilon$ on both ends, resulting in Eq. (16).

$$\frac{NTU_{m1}}{NTU_{m2}} = \frac{A_1^* \cdot St_{m1} \cdot Di_1^*}{A_2^* \cdot St_{m2} \cdot Di_2^*} \tag{14}$$

$$\ln\left(\frac{NTU_{m1}}{NTU_{m2}}\right) = \ln\left(\frac{A_1^*}{A_2^*} \frac{St_{m1}}{St_{m2}}\right) + \ln\left(\frac{Di_1^*}{Di_2^*}\right) \tag{15}$$

$$\Delta\varepsilon \cdot \frac{\ln\left(\frac{A_1^*}{A_2^*} \frac{St_{m1}}{St_{m2}}\right)}{\ln\left(\frac{NTU_{m1}}{NTU_{m2}}\right)} + \Delta\varepsilon \cdot \frac{\ln\left(\frac{Di_1^*}{Di_2^*}\right)}{\ln\left(\frac{NTU_{m1}}{NTU_{m2}}\right)} = \Delta\varepsilon \tag{16}$$

Here, the $\Delta\varepsilon$ on the right side of the equation represents the increase in single-pass efficiency due to the performance improvement. It can be decomposed into two terms on the left side: the first term represents the efficiency improvement due to $A^* \bullet St_m$, characterizing the contribution of enhanced mass transfer at the interface to the performance improvement. The second term represents the efficiency improvement due to Di^*, characterizing the contribution of internal diffusion strengthening to the improved performance. Thus, the enhancement of adsorption and purification performance resulting from these two aspects of mass transfer intensification can be examined separately.

3. Materials and experimental methods

3.1. Materials preparation for DIW

Chemicals and materials, including starch, carboxymethyl cellulose (CMC), bentonite clay, and polymethylmethacrylate (PMMA), were applied to prepare the ink for DIW, in which starch was bought from Dingxian Bio-Technology (Shanghai) Co., Ltd, CMC was provided by Topg Health Technology (Guangdong) Co., Ltd, bentonite clay was purchased from Beijing Merida Technology Co., Ltd, and PMMA was from HMHCL Materials (Dongguan) Co., Ltd.

The preparation process of the ink is described in detail in Supplementary *Section S2*. Generally, Ink #1 was obtained by thoroughly mixing deionized water, CMC, starch, and bentonite based on the method described in *Section S2*. Ink #1 was later heated to 70°C for 20 min to get Ink #2. PMMA particles, as template particles to generate multiple porous structures within adsorption materials, were added to Ink #2 with an amount of 4 g and mixed at 3600 r min^{-1} for 1 min by the planetary mixer. The final uniform suspension was named Ink #3. The rheological properties of Inks #1, #2, and #3 were systematically examined utilizing a rotational rheometer (MCR 302, Anton-Paar Instruments) equipped with a parallel plate geometry at a controlled temperature of 24°C.

3.2. Preparation of the net-like adsorption films with hierarchical porous structures

The DIW-printing schematic can be seen in Fig. 2(a), the process of which can be more intuitively seen in the video as the Supplementary material B. Ink #2 was employed in a bio-printer (Eazao, Bio) to produce two distinct film types: plane starch film (PSF) and net-like starch film (NSF). Ink #3 was utilized to fabricate NSF with an embedded particle template (NSFPT). The three films were fabricated via DIW onto

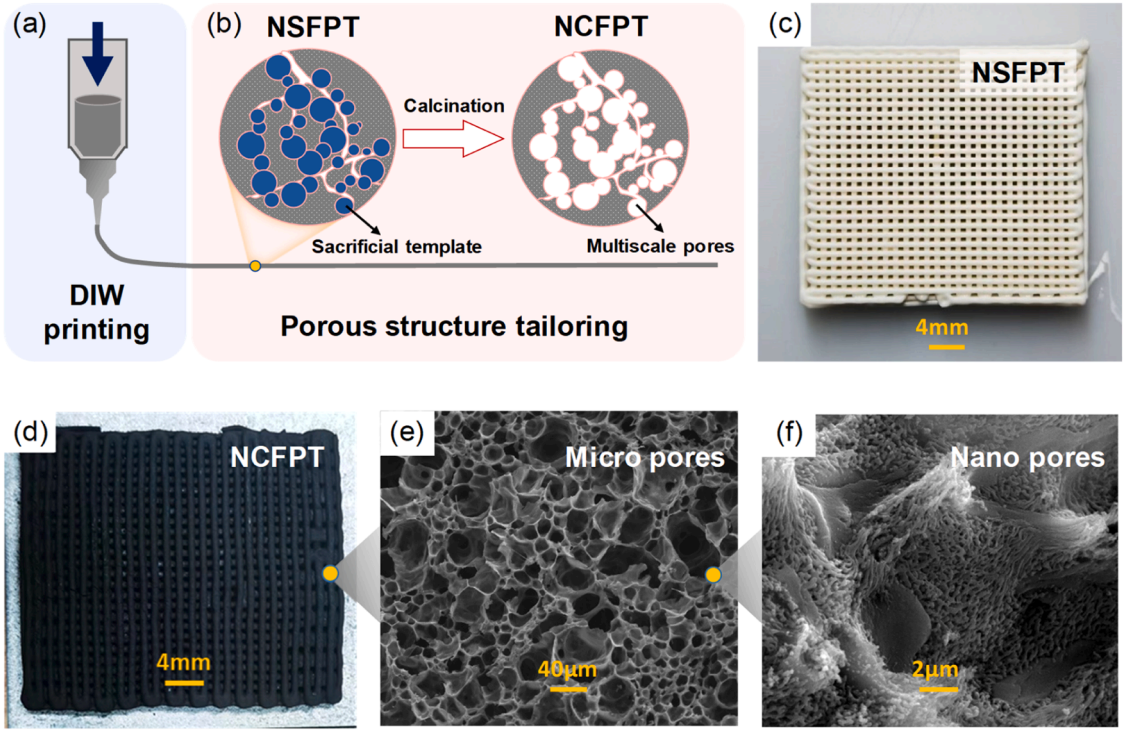

Fig. 2. The fabrication process of net-like adsorption film: (a) DIW printing and (b) porous structure tailoring using sacrificial template and carbonizing the starch to adsorptive carbon material simultaneously; The real pictures of the printed (c) net-like starch film with embedded particle template (NSFPT) and (d) net-like carbon-based adsorption films with additional porous structure (NCFPT); The SEM images of NCFPT at (e) 200 × and (f) 2000 × magnifications, respectively. The NSF0.4PT and NCF0.4PT were chosen as the typical ones for figures (c) to (f).

electrothermal polyimide circuit substrates (100 mm × 50 mm), and the film thicknesses were 2.5 mm. The printed starch films underwent drying in a vacuum freeze-drying machine (CHRIST, ALPHA 1–2 LD plus) for 10 h. Thereafter, these films were all calcinated in a positive pressure tube furnace (Tianjin ZhongRing Electric Furnace, SK-B05123K-00) under an argon atmosphere to produce carbon-based adsorbents from starch and porous structure by removing PMMA template particles (see Fig. 2(b) for details). The heating program for the tube furnace calcinating process is as follows: The temperature rose from 30°C to 500°C uniformly over 1.5 hours. A 2-hour hold was then conducted for PMMA-particle decomposition and initial starch carbonization. Then, the temperature rapidly increased to 800°C over 0.5 h and was kept for 1 hour to ensure complete carbonization and enhance the cross-linking between bentonite and carbon material. This process resulted in the transformation of PSF, NSF, and NSFPT into plane carbon-based adsorption films (PCF), net-like carbon-based adsorption films (NCF), and net-like carbon-based adsorption films with additional porous structure (NCFPT), respectively. NSFPT and NCFPT were selected as examples to illustrate the differences in adsorption films before and after calcination, summarized in Fig. 2(c) and (d).

The morphologies and 70 K nitrogen adsorption capacities of PCF, NCF, and NCFPT were characterized by field emission scanning electron microscopy (FE-SEM, ZEISS MultiSEM 505) and Nitrogen adsorption analyzer (Quantachrome autosorb iQ2), respectively. The nitrogen adsorption results were further used to quantitatively determine the pore distribution by Gaussian function [56]. The analytical formula is shown in Eq. (17).

$$\sum_{i=1}^{n} f_i(D) = \sum_{i=1}^{n} a_i \frac{1}{\sqrt{2\pi}\sigma_i} exp\left[-(logD - \mu_i)^2 \Big/ 2\sigma_i^2 \right] \quad (17)$$

where, n is the number of pore distributions; a_i represents the pore volume, cm^3/g; D and μ_i are the measured diameter and the mean diameter of the pores in log-coordinates, nm; σ_i is the standard deviation.

By adjusting the number and scale of PMMA template particles, various pore structures can be prepared for NCFPT adsorption films. We applied two sizes of template particles, under the diameters of 300 nm and 2 μm, to fabricate NCFPT films with different pore structures. The presence of 20 wt% and 40 wt% template particles under 300 nm diameter applied to adsorption films were named NCF0.2PT and NCF0.4PT, respectively. While another NCFPT film utilizing 40 wt% mixed 300-nm and 2-μm template particles (1:1) was named NCF0.4MPT. Based on NCF0.4MPT, 10 wt% more activated carbon particles with high specific surface area were added together with PMMA template particles to fabricate adsorption film. Then, we obtained the film named NCF0.4MPTAC.

3.3. Dynamic adsorption experiments and thermal regeneration

A schematic diagram describing the formaldehyde adsorption and thermal regeneration experimental platform is supplied in Supplementary Fig. S1. The dynamic formaldehyde adsorption experiments were executed utilizing an air channel measuring 450 mm in length, 70 mm in width, and 3 mm in thickness, on which the adsorption films were firmly fixed. The dynamic adsorption experiments were executed utilizing an air channel (450 mm×70 mm×3 mm). For the consistent generation of formaldehyde, a microfluidic controlled gas evaporation apparatus [57] was employed. The ambient air underwent a dual-stage purification process, first through a high-efficiency particulate air (HEPA) filter and subsequently via an activated carbon-packed pipe, before being channeled into a stainless-steel spiral tube within an insulated oil tank. As the rated operating conditions, a temperature-controlled heating system facilitated the extraction of the vaporized pollutants, creating a stream of polluted air with a constant 2 mg/m^3 concentration of formaldehyde. The polluted airflow was directed over the adsorption films, leading to the adsorption of pollutants. The 2 mg/m^3 introduced formaldehyde concentration is

approximately one-millionth of the saturated vapor concentration (5.64×10^6 mg/m^3), the value of which is calculated by EPI Suite v4.1 software. Thus, the adsorption process in this study aligns with the Langmuir adsorption isotherm regarding the thermodynamic aspects [58]. Theoretically, the partition coefficient of lower concentrations of formaldehyde on the adsorption film is the same as that of 2 mg/m^3 corresponding to this study [51]. It can be expected that a similar formaldehyde purification performance of the adsorption film as that at 2 mg/m^3 concentration will be obtained at a lower formaldehyde concentration.

The airflow rate was precisely maintained at 18.9 L/min by a mass flow controller (MC 20SLPM, Alicat Scientific, USA) for the formaldehyde adsorption experiments, ensuring the inlet air velocity at 1.5 m/s. The concentrations of formaldehyde before and after passing through the adsorption film (C_{in} and C_{out}) were quantified using a gas chromatography-barrier ionization discharge (GC-BID) detector (Shimazu, Nexis GC2030-BID, Japan), all within a controlled environmental chamber maintained at 20.0–26.0°C and 15 % ± 5 % relative humidity. The temperature range fell exactly within the requirements of the indoor air quality standard in China [59]. Meanwhile, Experiments were also designed to investigate the influence of humidity on formaldehyde adsorption performances. Under this case, the inlet air velocity was enlarged to 2.0 m/s for the convenience of humidity regulation. The relative humidity was adjusted as 15 %, 40 %, 60 %, and 85 %, respectively, for the experiments.

A 30-day experiment for formaldehyde adsorption was further carried out to verify long-term performance stability based on the thermal regeneration technology. After 8 hours of continuous formaldehyde adsorption, *in-situ* electrothermal regeneration was executed by applying a direct current (DC) regulated power supply (24 W at 20 V) to the PI circuit substrate, elevating the adsorbent temperature to 80°C for formaldehyde regeneration, with the heating process completing rapidly, in less than one minute [29]. The processes, including an 8-hour formaldehyde adsorption and a thermal regeneration, were regarded as one cycle and completed within one day.

The single-pass efficiency (ε) was calculated to reflect the formaldehyde purification capacities of adsorption films, calculated by Eq. (4). Meanwhile, another indicator used in this study to intuitively reflect the actual performance of the adsorption component is the effective adsorption capacity (EAC_{ad}, mg/g). This parameter represents the total adsorption of the component per unit mass before its performance diminishes to the point where it can no longer effectively control indoor pollution concentrations. The formula of EAC_{ad} can be seen as Eq. (18).

$$EAC_{ad} = \int_{t=0}^{t_e} \frac{G(C_{in} - C_{out})}{M} dt \tag{18}$$

where, t_e is the experimental time, h; G is the polluted air flow rate, m^3 s^{-1}; M is the adsorbent mass on adsorption film, g, the values of which can be seen in Supplementary *Section S3* for details. The EAC_{ad} parameter objectively evaluates the ability of the adsorption film to achieve effective pollutant control.

3.4. Comprehensive evaluation of the performance of adsorption films

The adsorption films developed in this study were compared with other formaldehyde purification components reported in the literature, which were retrieved from an online database following the method shown in Supplementary *Section S4*. Parameters for comprehensive evaluation of the formaldehyde purification performances are necessary when comparing the adsorption films in this study with others reported in the literature. To eliminate the influence of pollutant inlet concentration and adsorption component volume, we defined a parameter as the purification capacity (PA, g^{-1}), which is shown in Eq. (19).

$$PA = \frac{EAC_{ad}/C_{in}}{V_{com}} \tag{19}$$

where, the parameter, obtained as effective adsorption capacity (EAC_{ad}, mg/g) divided by the pollutant inlet concentration C_{in}, means the effective clean air volume per adsorbent mass, m^3/g; V_{com} represents the volume of the whole adsorption component, m^3. The PA parameter indicates the volume of clean air that can be achieved per unit volume of component and adsorbent mass. The larger the PA value, the stronger the purification capacity of the adsorption component.

The thermal regeneration characteristics of adsorbed thin-layer components allow the cumulative value of PA across multiple cycles to reach a high level. However, this benefit is not without cost, as the power consumption required for in-situ joule heating should be accounted for. Therefore, this study proposes a parameter as total power use per purification capacity (W^*, J·g), which considers both purification capacity and energy consumption, which represents the total energy consumption required to achieve PA per unit purification capacity. The energy consumption includes both fan energy consumption and regenerative energy consumption. W^* is calculated as Eq. (20).

$$W^* = \frac{W_{fan} + W_{heat}}{PA} \tag{20}$$

where, W_{fan} (J) is fan energy consumption and W_{heat} (J) is heating regenerative energy consumption. W^* can be used to evaluate the comprehensive performance of adsorbed thin-layer components, as well as to calculate the comprehensive energy consumption level of traditional adsorbed thin-layer components. This enables a performance comparison with adsorption film components. The PA and W^* parameters proposed in this study facilitate a more objective evaluation of the performance and energy efficiency of adsorption modules.

4. Results

4.1. Properties of the inks and adsorption films

4.1.1. Rheological properties of the inks

The viscosities of Inks #1 −#3 were illustrated in Fig. 3(a), all of which exhibit shear-thinning rheology characterized as a decline in viscosity as the shear rate increases. As the shear rate increases from 0.1 s^{-1} to 1000 s^{-1}, the viscosity of Ink #1 decreases from 7.1×10^5 mPa·s to 452 mPa·s, Ink #2 from 5.5×10^5 mPa·s to 776 mPa·s, and Ink #3 experiences a significant transition from 1.8×10^6 mPa·s to 797 mPa·s. The viscosities of all the inks are large enough to ensure that ink flow will not compromise the resolution achieved in DIW fabrication, thereby maintaining high print quality [60].

The viscoelastic characteristics of the inks, as depicted in Fig. 3(b), are crucial for the successful execution of DIW and the quality of the printed structures [22]. From Fig. 3(b), all inks exhibit high storage modulus (SM) at low shear stress, which diminishes progressively. Loss modulus (LMs) also decline with increasing shear stress but at lower decay rates compared to SMs, which thus maintains SM above LM at low-stress levels. This phase, dominated by elasticity, guarantees the ink is in a quasi-solid state and has resistance to deformation at a low shear rate. Conversely, at high shear stress, SM falls below LM, and the viscous property of ink dominates, causing the ink to behave like a liquid with good fluidity at a high extrusion rate. Notably, Ink #3 possesses a higher yield stress (the shear stress at the intersection of the SM curve and LM curve). When the ink is extruded out, and the shear stress generally decreases, Ink #3 exhibits solid material properties earlier, thereby mitigating flow deformation more effectively than Inks #1 and #2.

By comparing with the data reported in the literature, the inks prepared in this study exhibit excellent rheological properties as those in previous studies. There have been excellent studies preparing materials via DIW printing for constructing sensors [61,62], and redox splitting of

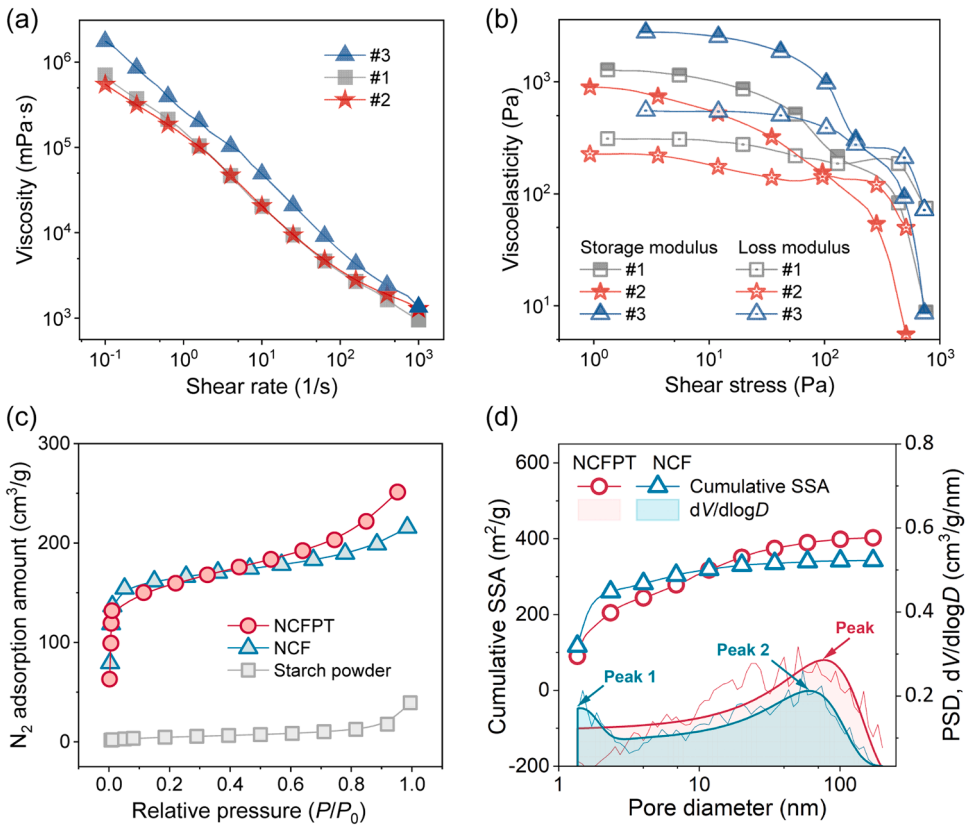

Fig. 3. (a) The viscosity and (b) the viscoelasticity of the prepared shear-thinning DIW inks #1–3; (c) the N_2 adsorption isothermals of starch powders, NCF and NCFPT, the experiments of which were carried out under 70 K; (d) the cumulative specific surface area (SSA) and pore size distribution (PSD) of NCF and NCFPT. The SSA and PSD were estimated using the Barret Joyner Halenda (BJH) method, determining pore size under 300 nm. The Gaussian fitting was conducted for pore distributions, the mean pore diameters (μ, nm) of which were then obtained for NCFPT (μ=77 nm) and NCF (μ_{Peak1}=1.4 nm; μ_{Peak2}=60 nm), respectively. The NCF0.4PT was chosen as the typical NCFPT for figures (c) and (d).

carbon dioxide [63]. The inks obtained in the literature reported similar decreasing tendencies of viscosity and viscoelastic characteristics as this work, the viscosity and viscoelasticity of which were determined as 10^1-10^7 mPa·s and 101–10^6 Pa, respectively. Nevertheless, researchers tended to apply expensive source materials and chemicals to prepare inks, which included triethanolamine and ammonium oleate [61], carrageenan composites with multi-wall carbon nanotubes [62], and pure ceria [63]. The use of these materials significantly increased the preparation cost. In comparison, the inks developed in this study mainly consist of starch, bentonite, and a trace amount of carboxymethyl cellulose with low preparation costs.

4.1.2. Surface morphology of adsorption films

The three variants of starch films, PSF, NSF, and NSFPT, were printed onto temperature-regulatable, flexible PI substrates as precursors for subsequent adsorption films [64]. The PSF is fabricated as a dense layer without any porous structures. The macroscopic structure of NSF is well consistent with NSFPT shown in Fig. 2(c) of the manuscript, revealing a multi-layered network with a homogenous structure, the filament diameters of which approximate 700 μm. The thicknesses of the three starch films are approximately 2.5 mm.

Subsequently, these starch films underwent carbonization, as delineated in Section 2.2.2, yielding PCF, NCF, and NCFPT, respectively. Fig. 2(c) of the manuscript displays the morphology of NCFPT (similar to NCF), which exhibits a uniformly structured carbonaceous net-like structure. Moreover, NCFPT features a gradient porous structure internally, which is depicted in the SEM images at 200 × and 2000 × magnification shown in Fig. 2(e) and (f), respectively. We also obtained SEM images at other magnifications for a better analysis of the multiscale porous structures within the adsorbents, as seen in Supplementary Fig. S2 for details. As reported in the literature, the main product obtained after the carbonization of starch is activated carbon with porous structures, which provides multiple adsorption sites for physical adsorption [45–47].

SEM characterization revealed that NCFPT possesses porous structures at multiple scales, with the scales ranging from 400 nm to 100 μm. The pore sizes between 200 nm and 400 nm are expected to originate predominantly from the thermal decomposition of the sacrificial template. The preparation method involved the addition of an excess of template particles, resulting in their non-uniform distribution within the material, not as isolated entities but rather in clusters. These clusters yield connected porous structures post-sintering, as evidenced in Fig. 2 (b) and (f). The formation of larger-scale pores, which do not correspond to the dimensions of the sacrificial template, is likely attributed to the high-temperature sintering and carbonization processes. During these processes, gases emitted from the decomposition of the sacrificial template and the carbonization of the starch migrate from the interior of the material, engendering pore structures spanning 2 μm to 100 μm. Moreover, these porous structures are interconnected, creating a porous network that facilitates rapid diffusion of gaseous pollutants within the material [65]. Thus, the multiscale porous structure of NCFPT perfectly matches the structural optimization design ideas raised in Section 2.1 of the manuscript, indicating porous structures ranged from macro- to nano-scales within the adsorption films.

4.1.3. Nitrogen adsorption capacities and pore distribution of adsorption films

Fig. 3(c) illustrates the adsorption isothermals of the raw starch

powders, NCF, and NCFPT for N_2, respectively. The surface morphologies and desorption isothermals of the materials are also summarized in Supplementary Fig. S3, respectively. The pristine starch material, serving as a precursor, exhibits negligible adsorption capacity. The N_2 adsorption amount of starch powders is less than 2 cm^2/g at a 0.1 relative pressure and two orders of magnitude lower than those of NCF and NCFPT, indicating that the starch powders have almost no adsorption sites for Langmuir adsorption. Thus, there are hardly any inner pores exist within starch powders for formaldehyde adsorption. The sintering process significantly enhances the adsorption capacities of the material. The equilibrium adsorption capacity of NCF approaches 240 m^3/g, while that of NCFPT is nearly 290 m^3/g. The comparison of the adsorption isotherms between NCF and NCFPT reveals a higher proportion of micropores in NCF, with adsorption capacity reaching approximately 70 % of the total at 0–0.05 relative pressure. In contrast, the pore size distribution of NCFPT is determined to be more uniform despite the substantial presence of nanopores. The proportion of mesopores and micropores is predicted to exceed that of NCF, resulting in a more rapid increase in the adsorption isotherm with increasing relative pressure. Thus, the NCFPT has superior N_2 adsorption and expected good formaldehyde purification performance, which is mainly reflected in higher adsorption capacity and more diverse pore structure.

The cumulative specific surface areas (SSA) and pore size distributions (PSD) of NCF and NCFPT were meticulously analyzed with a scale under 300 nm through the Barrett-Joyner-Halenda (BJH) method. As depicted in Fig. 3(d), the line scatter plot stands for the SSA results and the shaded area represents the data of PSD obtained by Gaussian fitting. NCFPT (403 m^2/g) has a larger cumulative SSA value than NCF (343 m^2/g). Specifically, Two obvious pore distribution peaks were observed in the NCF materials, with mean pore diameters (μ, nm) of 1.4 nm and 60 nm, respectively. Conversely, the PSD of NCFPT indicates a singular peak with a larger μ value of 77 nm. It means that sacrificial-template treatment removed small diameter pores and then created larger nanopores within the NCFPT. This process offers the possibility of enhancing the inner diffusion of pollutants inside the material (see Fig. 2 (f) for details). Considering that the SSA value of NCFPT did not decrease compared with NCF (and even slightly increased), the characteristic structure within the material remained intact after the sacrificial-template treatment. Therefore, the employment of the sacrificial template method introduces additional nanopores and mesopores to NCFPT, which has the potential to significantly enhance the mass transfer and purification kinetics of pollutants within the material.

4.2. Dynamic adsorption behaviors for formaldehyde

4.2.1. The formaldehyde removal performance

Fig. 4(a) presents the formaldehyde removal efficiency curves for PCF, NCF, and NCFPTs. As summarized in the *Experimental Section*, The NCFPT samples include NCF0.2PT, NCF0.4PT, NCF0.4MPT, and NCF0.4MPTAC, with the differences in the sizes and ratio of added template particles during fabrication. The column plots in the figure reveal that the initial formaldehyde removal efficiency of PCF is approximately 68.1 % at a head-on air velocity of 1.5 m/s. As time goes by, the efficiency of PCF diminishes progressively to 47.2 %, approximately 21 % lower than its initial efficiency. Thus, the PCF indicates a 2.74 mg/g EAC_{ad} (effective adsorption capacity) during the 8-hour formaldehyde adsorption, which can be seen in detail in Fig. 4(c). In contrast, the single-pass formaldehyde removal efficiency of NCF exceeds 75.8 % initially and then declines to around 57 %, with nearly a twice larger 8-hour EAC_{ad} as 4.27 mg/g. With the treatment by template particles, NCFPTs can be derived from NCF and have a higher formaldehyde removal efficiency of 78 % - 89 % initially, with less than 16 % efficiency decreases after 8-hour operations. The 8-hour EAC_{ad} of NCFPTs significantly increase to 7.50 mg/g – 8.60 mg/g, approximately twice larger than NCF.

The formaldehyde adsorption performances of NCFPTs can also be

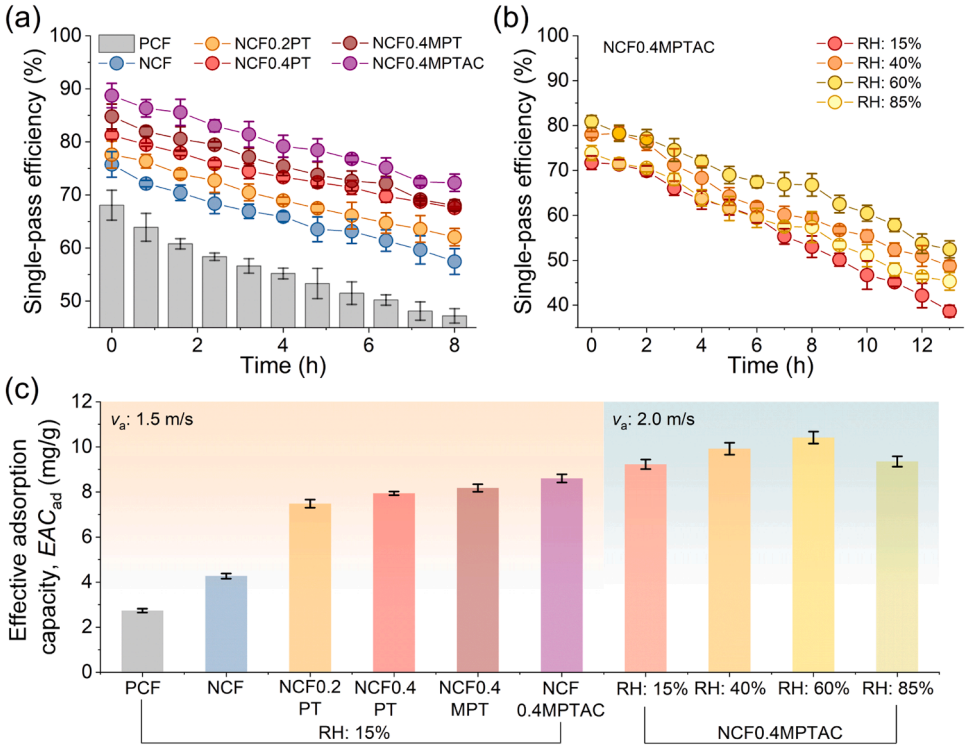

Fig. 4. (a) Variation of formaldehyde single pass removal efficiency over time for PCF, NCF, and NCFPT, respectively, with an inlet air velocity of 1.5 m/s and a relative humidity of 15 %. The NCFPT samples include NCF0.2PT, NCF0.4PT, NCF0.4MPT, NCF0.4MPTAC; (b) The formaldehyde removal performances of NCF0.4MPTAC under different relative humidity at an inlet air velocity of 2.0 m/s; (c) The 8-hour effective adsorption capacity (EAC_{ad}) of typical adsorption films under different inlet air velocities and relative humidities.

adjusted by modifying the quantity and size of sacrificial templates. With the treatment of 20 wt% 300nm-sacrificial template particles, the initial single-pass efficiency of NCF0.2PT is 77.6 %, which decays by 15.6 % after an 8-hour purification. When increasing the mass fraction of template particles to 40 wt%, the initial efficiency will be enhanced to 81.2 % for NCF0.4PT, revealing the improvement of pore distribution within the adsorbents. It is worth noting that the NCF0.4PT and NCF0.4MPT used the same mass ratios of template particles as 40 wt% for fabrication, but the initial performance of NCF0.4MPT is superior to that of NCF0.4PT, with an initial single-pass efficiency above 85 %. It may demonstrate that the use of mixed-scale template particles, particularly the addition of large particles to small ones, should have created a gradient multistage pore structure within NCF0.4MPT, reducing the tortuosity of the diffusion mass-transfer path of formaldehyde and thereby improving its initial adsorption performance compared to NCF0.4PT. However, the smaller number of template particles in NCF0.4MPT results in a less-developed pore structure compared to NCF0.4PT, leading to a rapid performance decline. After 8 hours, the performance of NCF0.4MPT declines more rapidly than that of NCF0.4PT, with a performance attenuation of 16.6 %.

As for NCF0.4MPTAC, the addition of high-specific surface-area activated carbon materials enhances the specific surface area of the material. This further improves the initial performance and adsorption potential of DIW printing adsorption films, with the highest single-pass efficiency of 89.0 % and also the largest 8-h EAC_{ad} of 8.60 mg/g among all the adsorption films. However, the addition of activated carbon materials did not significantly mitigate the performance attenuation. The single-pass efficiency decreased by 16.4 % due to the accumulation of interface pollutant concentration.

4.2.2. *Effect of humidity on the formaldehyde removal performance*

The effect of water vapor on the properties of adsorbed materials has been studied extensively, revealing that relative humidity significantly impacts the VOC adsorption behavior on adsorbent materials [66]. In this study, we examined the influence of humidity on the formaldehyde adsorption process by multi-scale adsorption films. The NCF0.4MPTAC was selected as the target adsorption film for the experiments, considering its outstanding formaldehyde purification performances, and the inlet air velocity was controlled at 2.0 m/s for the convenience of humidity adjustment.

Fig. 4(b) shows the results of formaldehyde purification performance under different humidity. At 15 % relative humidity, the single-pass efficiency of formaldehyde was 71.7 % at an inlet air velocity of 2.0 m/s, the efficiency of which is relatively lower than that of 1.5 m/s. High velocity reduces the duration of formaldehyde contact with adsorption film, resulting in a lower single-pass efficiency, but it can also enhance air disturbance and mass-transfer capacity. Thus, the 8-hour EAC_{ad} of the experiment under 2.0 m/s is relatively larger than that of 1.5 m/s, as shown in Fig. 4(c). As the relative humidity increased to 40 %, the formaldehyde adsorption performance significantly improved, with the initial passing efficiency reaching nearly 78 %. The purification efficiency remained higher than at 15 % relative humidity throughout the more than 12-hour purification process, with an 8-hour EAC_{ad} calculated as 9.22 mg/g. At 60 % relative humidity, the formaldehyde purification performance improved further, and the initial single-pass efficiency exceeded 80 %, the 8-hour EAC_{ad} of which reached 10.4 mg/g. The possible reason for this trend is that increased humidity infiltrates the adsorptive material, enhancing the affinity for formaldehyde and promoting the adsorption process [67]. Further increases in relative humidity may lead to the formation of water films in microporous structures where the saturated vapor pressure of water is reduced due to capillary action [14], causing water vapor to liquefy and form water films at high humidity [68,69]. These water films facilitate the absorption of formaldehyde.

However, when the relative humidity increased to 85 %, the formaldehyde adsorption performance decreased sharply to 9.35 mg/g of 8-hour EAC_{ad}, but still slightly higher than at 15 % relative humidity. It may be due to the competitive adsorption of water vapor and formaldehyde. When the humidity is excessively high, water vapor and formaldehyde as polar molecules would competitively adsorb on the interface of adsorbents, slightly impeding the formaldehyde adsorption process. The results are consistent with those reported by Pei et al [70]. The enhancement of relative humidity on formaldehyde purification by adsorption films further indicates significant applicability in actual indoor environments.

4.2.3. *The 30-day experiment of adsorption and desorption on formaldehyde*

Thermal regeneration is expected to restore the performance of the adsorption films effectively. We applied NCF0.4MPTAC to explore the potential of improving formaldehyde purification performance via long-term dynamic thermal regeneration. A 30-day adsorption-desorption cycle experiment was carried out, with each cycle consisting of 8 hours of adsorption and purification followed by 1 hour of desorption for a total of 30 cycles.

The experimental results are presented in Fig. 5(a). The initial adsorption efficiency of the thin-layer components reached 90 %. Over the 30-day period, which included more than 250 hours of adsorption-regeneration cycles, the single-pass efficiency of the thin-layer components consistently remained above 65 %. Fig. 5(b) presents a box plot summarizing the single-pass efficiency and effective adsorption capacity for each purification cycle. The results demonstrate a slight downward oscillation in efficiency during the 30-day adsorption-desorption cycle, but the trend is not pronounced. After 30 days, the average single-pass efficiency attenuation was less than 10 %, while the median attenuation was less than 8 %. As illustrated in Fig. 5(b), the single-pass efficiency of the first five cycles gradually decreased. From the 6th cycle onwards, the efficiency curve displayed an oscillating trend, with the decline in efficiency being suppressed. Between the 5th and 30th days, the median single-pass efficiency decreased by only 4 %. This observation suggests that continuous heating at 80°C for 1 hour effectively restored the performance of the adsorbed thin-layer components.

The average effective adsorption capacity, EAC_{ad}, of 8-hour adsorption purification in 30 cycles is about 8.06 mg/g. Throughout the 30 cycles, the adsorption capacity of the thin layer remained relatively stable, with an attenuation rate of no more than 10 %. The limited attenuation in formaldehyde adsorption performance also indicates that the macro- and inner-pore structures remain unchanged during thermal regenerations, revealing good mechanical properties of the carbonaceous adsorption films. The good mechanical properties of the adsorption films can also be directly verified in our previous research [57]. Especially, the 80℃ regeneration temperature is much lower than the spontaneous ignition temperature and the point of initial oxidation of adsorbents, which are determined as more than 300℃ according to Suzin et al. [71]. Thus, the mechanical properties of the carbonaceous adsorption films are proven to be acceptable for indoor formaldehyde purification cooperated with thermal regeneration. Considering the performance recovery brought by regeneration, the cumulative total adsorption capacity of 30 cycles reached approximately 241.7 mg/g, which is significantly higher than the formaldehyde purification amounts of technologies reported in most existing studies. Thus, the application of thermal regeneration greatly enhances the formaldehyde purification potential of adsorption films.

5. Discussion

5.1. *Attribution analysis for the performance improvement of adsorption films*

The improvement in formaldehyde purification performance of NCF and NCFPT compared to PCF can be quantitatively attributed to two factors: interfacial mass transfer enhancement and internal diffusion

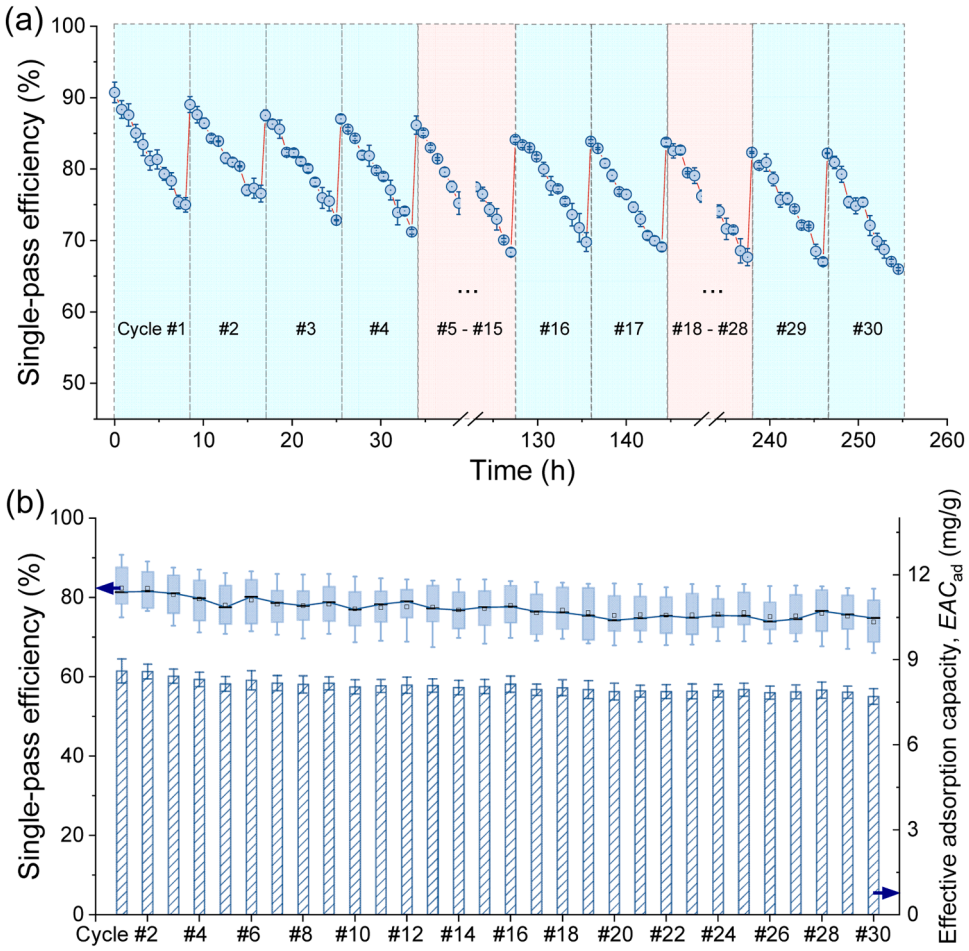

Fig. 5. (a) Adsorption and thermal-regeneration cycles of NCF0.4MPTAC on formaldehyde for 30 days, including 8-hour adsorption and 1-hour regeneration per day. (b) The single-pass efficiency and effective adsorption capacity, EAC_{ad}, of NCF0.4MPTAC over time. The adsorption experiments were carried out under the environmental conditions of temperature 20–26℃, inlet air velocity 1.5 m/s, and relative humidity 20 %-30 %, while the temperature, inlet air velocity, and relative humidity of desorption experiments were 80℃, 0.3 m/s and < 10 %, respectively.

enhancement, which can be represented by $A^*\bullet St_m$ and Di^*, respectively. We calculated both of the two parameters to analyze the quantitative attributions of performance improvements, for which the NCF0.4MPTAC was selected as the typical NCFPT due to its outstanding performance. Details about the calculation process are shown in Supplementary *Section S5*.

Then, the contributions of $A^*\bullet St_m$ and Di^* parameters to the single-pass-efficiency improvement can be obtained for NCF and NCF0.4MPTAC by Eq. (16), represented as $\Delta\varepsilon_{A^*\bullet Stm}$ and $\Delta\varepsilon_{Di^*}$ in Fig. 6 (a). The gray, orange, and red columns indicate the single-pass efficiency of PCF, NCF, and NCF0.4MPTAC, respectively. The cyan columns represent the increase in adsorption properties attributable to interfacial mass transfer enhancement (i.e., the enhancement of $A^*\bullet St_m$), and the blue columns represent mass transfer enhancement through internal diffusion within the material (i.e., the increase in Di^*). From the performance comparison results between NCF and PCF, it is evident that enhanced interfacial mass transfer is the primary reason for the performance improvement. The increase in $A^*\bullet St_m$ resulted in a 5.05 % performance improvement, the value of which is only 2.63 % caused by the increase in Di^*. In the performance comparison between NCF0.4MPTAC and PCF, the increases in $A^*\bullet St_m$ and Di^* resulted in 4.53 % and 16.1 % performance improvements, respectively. It means that the nanoscale interconnected pore structures within NCF0.4MPTAC effectively enhance interfacial mass diffusion.

5.2. Performance comparisons with the existing studies and commercial products

Performance comparisons were conducted for the adsorption films developed in this study, along with existing studies that considered formaldehyde adsorption capacity. As for the materials reported in the literature, we classified them into two groups: pure physical adsorption and physical + chemical adsorption. The purification capacities (*PA*, g^{-1}) of the studies were calculated for the convenience of comparison. The data and references can be seen in detail in Supplementary Table S3. Upon calculating *PA*, we classified the studies into two categories based on the type of materials used: pure physical adsorption (physisorption in short) and physical + chemical adsorption (chemisorption in short). The calculated *PA* results are shown in Fig. 6(b), details of which can also be seen in Supplementary Table S3. The multi-scale adsorption films in this study demonstrate outstanding purification flux and superior purification capacity compared with the reported adsorbents. The NCF exhibits excellent formaldehyde purification capacity (*PA*) higher than nearly all the physisorption and most chemisorption groups, as shown in the green region of Fig. 6(b). In comparison, the *PA* of NCF0.4PTMAC is even the highest among all the physisorption and chemisorption groups except for extremely few studies (see the blue region of Fig. 6(b) for details). Especially, the airflow rates applied in this study are nearly 1–3 orders of magnitude larger than the others, indicating an outstanding purified air generation rate and application potential.

This study also investigated well-known domestic and foreign brands

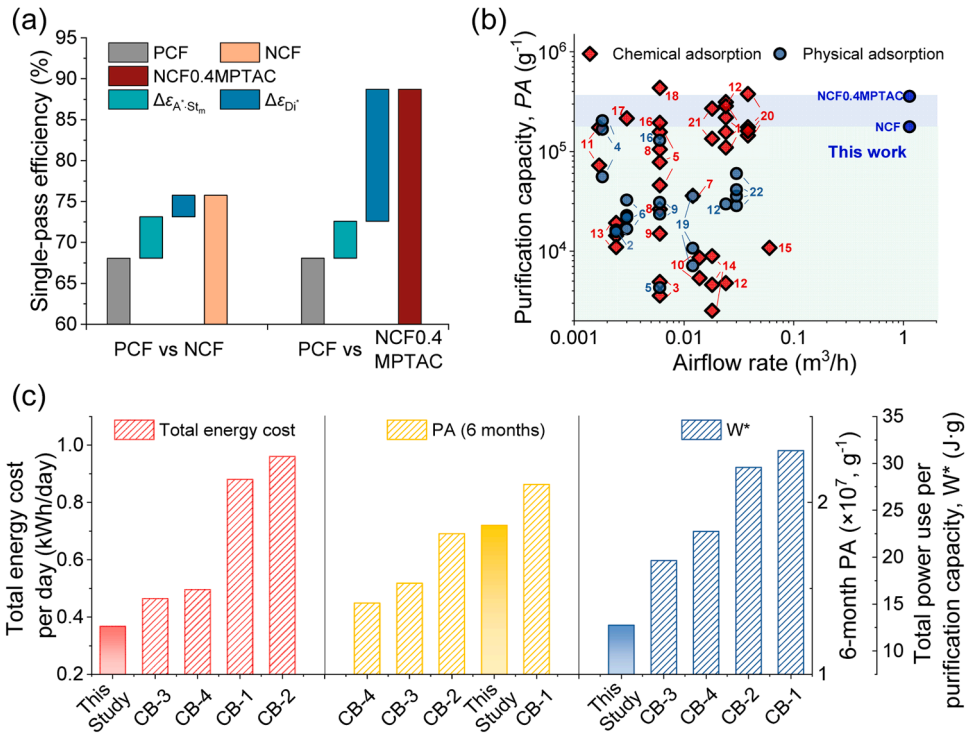

Fig. 6. (a) The $A^*{\cdot}St_m$ and Di^* attributing results for the single-pass efficiency gains of NCF and NCF0.4MPTAC over PCF. The parameters $A^*{\cdot}St_m$ and Di^* represent the effects of interfacial mass transfer and internal diffusion on formaldehyde adsorption, respectively; (b) Comparisons of formaldehyde purification capacity (*PA*) as well as airflow rate between NCF/NCF0.4MPTAC and other adsorbents in existing literature. The reference can be seen in detail in Supplementary Table S3; (c) Comparisons of performance and comprehensive energy consumption of NCF0.4MPTAC with well-known purification equipment products. The abbreviation 'CB' in the figure means 'commercial brand'.

of air purification products, selecting two notable domestic and two foreign brands of purification equipment online (www.jd.com). All four products possess the capability to purify particulate matter and formaldehyde, with specified Clean Air Delivery Rate (*CADR*) values for these pollutants. By using the relationship between *CADR*, air volume, and single-pass efficiency and assuming the single-pass efficiency for particulate matter is 100 % (in reality, it is generally above 99 %, making the error negligible), we calculated the air volume of the purification equipment. Subsequently, the single-pass efficiency for formaldehyde purification was determined based on the air volume and the *CADR* for formaldehyde purification. Applying the provided parameters such as lifespan, equipment volume, and rated power by manufacturers, we then obtained and further compared the *PA* and comprehensive energy consumption factor (W^*) of the multi-scale adsorption film, NCF0.4MPTAC, and the four purification products over a half-year purification control cycle. The results are depicted in Fig. 6(c), the data and calculation process of which can be seen in Supplementary Table S4. NCF0.4MPTAC exhibits a total energy cost of 0.37 kW·h per day, which is the lowest among all the purification equipment ranging from 0.46 kW·h to 0.96 kW·h. Meanwhile, the formaldehyde purification performance of NCF0.4MPTAC is the second highest, revealing outstanding cost-effectiveness even compared with commercial products. The excellent formaldehyde purification performance of NCF0.4MPTAC combined with low energy cost should result in its extremely low resistance and low in-situ heating regenerative energy consumption. According to the proposed W^* parameter (total power use per purification capacity), NCF0.4MPTAC indicates a W^* value of 12.7 W·g, which is several times lower than the other commercial equipment and evidences substantial application potential.

6. Conclusions

In this study, we have proposed carbonaceous net-like adsorption films with multiscale porous structures that are excellent in formaldehyde purification by demonstrating high efficiency and large effective adsorption capacity. We have introduced key dimensionless parameters, $A^*{\cdot}St_m$ and Di^*, to quantify the influences of interfacial mass-transfer intensity and internal diffusion on pollutant removal performance. Guided by the optimal $A^*{\cdot}St_m$ and Di^* parameters, we have optimized the structures within adsorption films by combining the DIW-printing and sacrificial template, focusing on creating macro- and mesoscale meshes on the film surface and developing micro- to nano-scale pores inside the sorption materials. Compared to unmodified planar adsorption films, the optimized adsorption films achieve the initial single-pass efficiency of formaldehyde, increasing from 68.1 % to 89.0 %. The effective adsorption capacity, EAC_{ad}, has seen a substantial rise from 2.74 mg/g to 8.60 mg/g. When applying thermal regeneration, the multi-scale adsorption films can be stably operated for 30 days, significantly enlarging the EAC_{ad} to a much larger value of 241.7 mg/g in comparison with existing studies. Moreover, through performance comparisons with other studies and commercial products, the multi-scale adsorption film has shown nearly the highest purification rate and capacity among physisorption and chemisorption technologies with 1–3 orders of magnitude larger airflow rates. The long-term operating energy cost is as low as 0.37 kW·h per day and several times lower than the other commercial products, evidencing substantial application potential. The design and fabrication of the multi-scale adsorption film offer a promising avenue for efficient formaldehyde removal, catering to the practical needs of indoor air purification, carbon capture, and gas separation in the field of environmental engineering.

CRediT authorship contribution statement

Zhuo Chen: Writing – review & editing, Writing – original draft, Validation, Supervision, Methodology, Investigation, Data curation. **Yan Wang:** Writing – original draft, Validation, Investigation. **Qiwei**

Chen: Validation, Methodology, Investigation, Data curation. **Wuwei Zou:** Writing – review & editing, Validation, Data curation. **Jinhan Mo:** Writing – review & editing, Writing – original draft, Validation, Supervision, Methodology, Funding acquisition, Conceptualization. **Yuan Li:** Supervision, Data curation.

Declaration of Competing Interest

The authors declare that they have no known competing financial interests or personal relationships that could have appeared to influence the work reported in this paper.

Acknowledgment

This work was financially supported by the National Natural Science Foundation of China (No. 52325801).

Appendix A. Supporting information

Supplementary data associated with this article can be found in the online version at doi:10.1016/j.jhazmat.2025.137203.

Data availability

Data will be made available on request.

References

[1] Xia, F., Chen, Z., Tian, E., Mo, J., 2024. A super sandstorm altered the abundance and composition of airborne bacteria in Beijing. J Environ Sci 144, 35–44. https://doi.org/10.1016/j.jes.2023.07.029.
[2] Xia, F., Chen, Z., Gao, Y., Tian, E., Mo, J., 2024. Simultaneous capture and inactivation of airborne bacteria by a dual-zone electrostatically actuated filter. ACS EST Eng 4 (4), 987–994. https://doi.org/10.1021/acsestengg.3c00525.
[3] Gao, Y., Wang, J., Tian, E., Chen, Z., Mo, J., 2025. Electric-field activating on-surface tailored (OST) coarse polyester fibers for efficient airborne particle removal: interfacial morphologies and electrical response. Sep Purif Technol 353, 128291. https://doi.org/10.1016/j.seppur.2024.128291.
[4] Chen, Z., Xia, F., Fan, Y., Jiang, Y., Xu, Y., Mo, J., 2024. Partitioning mechanisms and film formations of DEHP on realistic indoor airborne particles and road dust. Build Environ 252, 111273. https://doi.org/10.1016/j.buildenv.2024.111273.
[5] Chen, Z., Gao, Y., Xia, F., Bi, C., Mo, J., 2024. Formation kinetics of SVOC organic films and their impact on child exposure in indoor environments. Sci Total Environ 912, 168970. https://doi.org/10.1016/j.scitotenv.2023.168970.
[6] Wang, Y., Chen, Z., Chen, Q., Tian, E., Han, N., Mo, J., 2024. Preconcentrating sensor systems toward indoor low-concentration VOC detection by goal-oriented, sequential, inverse design strategy. Build Environ 254, 111372. https://doi.org/10.1016/j.buildenv.2024.111372.
[7] Liu, N., Liu, W., Deng, F., Liu, Y., Gao, X., Fang, L., et al., 2023. The burden of disease attributable to indoor air pollutants in China from 2000 to 2017. Lancet Planet Health 7 (11), e900–e911. https://doi.org/10.1016/S2542-5196(23)00215-2.
[8] Li, Y., Wei, M., Wei, W., Zhang, W., Liu, L., 2023. Feasibility of soil oxidation-reduction potential in judging shear behaviour of hydrocarbon-contaminated soil. J Environ Manag 342, 118303. https://doi.org/10.1016/j.jenvman.2023.118303.
[9] Hun, D.E., Corsi, R.L., Morandi, M.T., Siegel, J.A., 2010. Formaldehyde in residences: long-term indoor concentrations and influencing factors. Indoor Air 20 (3), 196–203. https://doi.org/10.1111/j.0905-6947.2010.00644.x.
[10] Chen, Z., Chen, Q., Xu, Y., Mo, J., 2022. Partitioning characteristics of indoor VOCs on impermeable surfaces covered by film-phase DnBP and DEHP. J Hazard Mater Adv 8, 100191. https://doi.org/10.1016/j.hazadv.2022.100191.
[11] Zou, W., Wang, Y., Tian, E., Wei, J., Peng, J., Mo, J., 2024. A new dynamic and vertical photovoltaic integrated building envelope for high-rise glaze-facade buildings. Engineering 39, 194–203. https://doi.org/10.1016/j.eng.2024.01.014.
[12] Bradman, A., Gaspar, F., Castorina, R., Williams, J., Hoang, T., Jenkins, P.L., et al., 2017. Formaldehyde and acetaldehyde exposure and risk characterization in California early childhood education environments. Indoor Air 27 (1), 104–113. https://doi.org/10.1111/ina.12283.
[13] Du, Z., Mo, J., Zhang, Y., 2014. Risk assessment of population inhalation exposure to volatile organic compounds and carbonyls in urban China. Environ Int 73, 33–45. https://doi.org/10.1016/j.envint.2014.06.014.
[14] Chen, Z., Wu, Q., Xu, Y., Mo, J., 2022. Partitioning of airborne PAEs on indoor impermeable surfaces: A microscopic view of the sorption process. J Hazard Mater 424 (Pt A), 127326. https://doi.org/10.1016/j.jhazmat.2021.127326.
[15] Gao, Y., Tian, E., Mo, J., 2023. Electrostatic polydopamine-interface-mediated (e-PIM) filters with tuned surface topography and electrical properties for efficient particle capture and ozone removal. J Hazard Mater 441, 129821. https://doi.org/10.1016/j.jhazmat.2022.129821.
[16] Li, Y., Tu, C., Wei, M., Liu, L., Zhang, W., 2024. Remediation effectiveness of aging diesel-contaminated soil using thermochemical treatment: soil microstructure transformation and reusability. J Clean Prod 452, 142232. https://doi.org/10.1016/j.jclepro.2024.142232.
[17] Zhang, Y., Mo, J., Li, Y., Sundell, J., Wargocki, P., Zhang, J., et al., 2011. Can commonly-used fan-driven air cleaning technologies improve indoor air quality? A literature review. Atmos Environ 45 (26), 4329–4343. https://doi.org/10.1016/j.atmosenv.2011.05.041.
[18] Chen, Z., Tian, E., Mo, J., 2020. Removal of gaseous DiBP and DnBP by ionizer-assisted filtration with an external electrostatic field. Environ Pollut 267, 115591. https://doi.org/10.1016/j.envpol.2020.115591.
[19] Gil, R.R., Ruiz, B., Lozano, M.S., Martín, M.J., Fuente, E., 2014. VOCs removal by adsorption onto activated carbons from biocollagenic wastes of vegetable tanning. Chem Eng J 245, 80–88. https://doi.org/10.1016/j.cej.2014.02.012.
[20] Jeon, J., Park, J.H., Wi, S., Yun, B.Y., Kim, T., Kim, S., 2020. Field study on the improvement of indoor air quality with toluene adsorption finishing materials in an urban residential apartment. Environ Pollut 261, 114137. https://doi.org/10.1016/j.envpol.2020.114137.
[21] Davó-Quiñonero, A., Sorolla-Rosario, D., Bailón-García, E., Lozano-Castelló, D., Bueno-López, A., 2019. Improved asymmetrical honeycomb monolith catalyst prepared using a 3D printed template. J Hazard Mater 368, 638–643. https://doi.org/10.1016/j.jhazmat.2019.01.092.
[22] Chen, Q., Tian, E., Wang, Y., Mo, J., Xu, G., Zhu, M., 2023. Recent progress and perspectives of direct ink writing applications for mass transfer enhancement in gas-phase adsorption and catalysis. Small Methods 7, 2201302. https://doi.org/10.1002/smtd.202201302.
[23] Chen, Z., Afshari, A., Mo, J., 2020. A method using porous media to deliver gas-phase phthalates rapidly and at a constant concentration: effects of temperature and media. Environ Pollut 262, 113823. https://doi.org/10.1016/j.envpol.2019.113823.
[24] Zhu, J., Wu, P., Chao, Y., Yu, J., Zhu, W., Liu, Z., et al., 2022. Recent advances in 3D printing for catalytic applications. Chem Eng J 433, 134341. https://doi.org/10.1016/j.cej.2021.134341.
[25] Kearns, E.R., Gillespie, R., D'Alessandro, D.M., 2021. 3D printing of metal–organic framework composite materials for clean energy and environmental applications. J Mater Chem A 9 (48), 27252–27270. https://doi.org/10.1039/d1ta08777k.
[26] Hasan, F.A., Xiao, P., Singh, R.K., Webley, P.A., 2013. Zeolite monoliths with hierarchical designed pore network structure: synthesis and performance. Chem Eng J 223, 48–58. https://doi.org/10.1016/j.cej.2013.02.100.
[27] Rezaei, F., Webley, P., 2010. Structured adsorbents in gas separation processes. Sep Purif Technol 70 (3), 243–256. https://doi.org/10.1016/j.seppur.2009.10.004.
[28] Chen, H., Mo, J., Xiao, R., Tian, E., 2019. Gaseous formaldehyde removal: a laminated plate fabricated with activated carbon, polyimide, and copper foil with adjustable surface temperature and capable of in situ thermal regeneration. Indoor Air 29 (3), 469–476. https://doi.org/10.1111/ina.12540.
[29] Chen, Q., Xiao, R., Lei, X., Yu, T., Mo, J., 2021. Experimental and modeling investigations on the adsorption behaviors of indoor volatile organic compounds in an in-situ thermally regenerated adsorption-board module. Build Environ 203, 108065. https://doi.org/10.1016/j.buildenv.2021.108065.
[30] Ji, D., Lin, Y., Guo, X., Ramasubramanian, B., Wang, R., Radacsi, N., et al., 2024. Electrospinning of nanofibres. Nat Rev Methods Prim 4 (1), 1. https://doi.org/10.1038/s43586-023-00278-z.
[31] Oh, G.-Y., Ju, Y.-W., Kim, M.-Y., Jung, H.-R., Kim, H.J., Lee, W.-J., 2008. Adsorption of toluene on carbon nanofibers prepared by electrospinning. Sci Total Environ 393 (2), 341–347. https://doi.org/10.1016/j.scitotenv.2008.01.005.
[32] Liu, Z., Ma, Z., Pang, X., Ahmad, M., Zhao, Y., Su, N., et al., 2023. Electrospinning prepared nickel-based carbon fibers with enhanced adsorption capacity for adsorption desulfurization of fuels. Chem Eng J 478, 147254. https://doi.org/10.1016/j.cej.2023.147254.
[33] Cui, J., Li, F., Wang, Y., Zhang, Q., Ma, W., Huang, C., 2020. Electrospun nanofiber membranes for wastewater treatment applications. Sep Purif Technol 250, 117116. https://doi.org/10.1016/j.seppur.2020.117116.
[34] Agarwal, S., Greiner, A., Wendorff, J.H., 2013. Functional materials by electrospinning of polymers. Prog Polym Sci 38 (6), 963–991. https://doi.org/10.1016/j.progpolymsci.2013.02.001.
[35] Lawson, S., Alwakwak, A.-A., Rownaghi, A.A., Rezaei, F., 2020. Gel–print–grow: a new way of 3D printing metal–organic frameworks. ACS Appl Mater Interfaces 12 (50), 56108–56117. https://doi.org/10.1021/acsami.0c18720.
[36] Thakkar, H., Lawson, S., Rownaghi, A.A., Rezaei, F., 2018. Development of 3D-printed polymer-zeolite composite monoliths for gas separation. Chem Eng J 348, 109–116. https://doi.org/10.1016/j.cej.2018.04.178.
[37] Wang, S., Bai, P., Sun, M., Liu, W., Li, D., Wu, W., et al., 2019. Fabricating mechanically robust binder-free structured zeolites by 3D printing coupled with zeolite soldering: a superior configuration for CO2 capture. Adv Sci 6 (17), 1901317. https://doi.org/10.1002/advs.201901317.
[38] Zhu, C., Qi, Z., Beck, V.A., Luneau, M., Lattimer, J., Chen, W., et al., 2018. Toward digitally controlled catalyst architectures: hierarchical nanoporous gold via 3D printing. Sci Adv 4 (8), eaas9459. https://doi.org/10.1126/sciadv.aas9459.
[39] Chen, Z., Li, Z., Li, J., Liu, C., Lao, C., Fu, Y., et al., 2019. 3D printing of ceramics: a review. J Eur Ceram Soc 39 (4), 661–687. https://doi.org/10.1016/j.jeurceramsoc.2018.11.013.
[40] Corker, A., Ng, H.C., Poole, R.J., Garcia-Tunon, E., 2019. 3D printing with 2D colloids: designing rheology protocols to predict 'printability' of soft-materials. Soft Matter 15 (6), 1444–1456. https://doi.org/10.1039/c8sm01936c.

[41] Wang, S., Bai, P., Wei, Y., Liu, W., Ren, X., Bai, J., et al., 2019. Three-dimensional-printed core-shell structured MFI-type zeolite monoliths for volatile organic compound capture under humid conditions. ACS Appl Mater Interfaces 11 (42), 38955–38963. https://doi.org/10.1021/acsami.9b13819.
[42] Luo, J., Liu, B., Shi, R., Guo, Y., Feng, Q., Liu, Z., et al., 2021. The effects of nitrogen functional groups and narrow micropore sizes on CO2 adsorption onto N-doped biomass-based porous carbon under different pressure. Microporous Mesoporous Mater 327, 111404. https://doi.org/10.1016/j.micromeso.2021.111404.
[43] Wang, H., Zhang, R., Yuan, D., Xu, S., Wang, L., 2020. Gas foaming guided fabrication of 3D porous plasmonic nanoplatform with broadband absorption, tunable shape, excellent stability, and high photothermal efficiency for solar water purification. Adv Funct Mater 30 (46), 2003995. https://doi.org/10.1002/adfm.202003995.
[44] Cai, T., Sun, H., Qiao, J., Zhu, L., Zhang, F., Zhang, J., et al., 2021. Cell-free chemoenzymatic starch synthesis from carbon dioxide. Science 373 (6562), 1523–1527. https://doi.org/10.1126/science.abh4049.
[45] Zhao, S., Wang, C.-Y., Chen, M.-M., Wang, J., Shi, Z.-Q., 2009. Potato starch-based activated carbon spheres as electrode material for electrochemical capacitor. J Phys Chem Solids 70 (9), 1256–1260. https://doi.org/10.1016/j.jpcs.2009.07.004.
[46] Li, M., Bi, Z., Xie, L., Sun, G., Liu, Z., Kong, Q., et al., 2019. From starch to carbon materials: insight into the cross-linking reaction and its influence on the carbonization process. ACS Sustain Chem Eng 7 (17), 14796–14804. https://doi.org/10.1021/acssuschemeng.9b02821.
[47] Suo, F., Liu, X., Li, C., Yuan, M., Zhang, B., Wang, J., et al., 2019. Mesoporous activated carbon from starch for superior rapid pesticides removal. Int J Biol Macromol 121, 806–813. https://doi.org/10.1016/j.ijbiomac.2018.10.132.
[48] Zhou, X., Liu, C.-J., 2020. Three-dimensional printing of porous carbon structures with tailorable pore sizes. Catal Today 347, 2–9. https://doi.org/10.1016/j.cattod.2018.05.044.
[49] Mo, J., Zhang, Y., Yang, R., 2005. Novel insight into VOC removal performance of photocatalytic oxidation reactors. Indoor Air 15 (4), 291–300. https://doi.org/10.1111/j.1600-0668.2005.00374.x.
[50] Lei, X., Chen, Q., Wang, Y., Mo, J., 2023. Modelling and implementation of an in-situ thermally regenerated adsorption module for removing gaseous xylene. Build Environ 236, 110275. https://doi.org/10.1016/j.buildenv.2023.110275.
[51] Xia, G., Ball, W.P., 1999. Adsorption-partitioning uptake of nine low-polarity organic chemicals on a natural sorbent. Environ Sci Technol 33 (2), 262–269. https://doi.org/10.1021/es980581g.
[52] Wang, J., Guo, X., 2020. Adsorption kinetic models: physical meanings, applications, and solving methods. J Hazard Mater 390, 122156. https://doi.org/10.1016/j.jhazmat.2020.122156.
[53] Incropera, F.P., DeWitt, D.P., Bergman, T.L., Lavine, A.S., 1996. Fundamentals of heat and mass transfer. Wiley, New York.
[54] Qian, K., Zhang, Y., Little, J.C., Wang, X., 2007. Dimensionless correlations to predict VOC emissions from dry building materials. Atmos Environ 41 (2), 352–359. https://doi.org/10.1016/j.atmosenv.2006.07.042.
[55] Cao, J., Weschler, C.J., Luo, J., Zhang, Y., 2016. Cm-history method, a novel approach to simultaneously measure source and sink parameters important for estimating indoor exposures to phthalates. Environ Sci Technol 50 (2), 825–834. https://doi.org/10.1021/acs.est.5b04404.
[56] Wei, M., Wei, W., Li, Y., Liu, L., Zhong, F., Xue, Q., 2023. Maximizing the pozzolanic potential of superfine iron tailings for low-carbon stabilization: application of high-calcium geopolymer. Resour Conserv Recycl 198, 107198. https://doi.org/10.1016/j.resconrec.2023.107198.
[57] Chen, Q., Tian, E., Luo, Z., Mo, J., 2022. Adsorption film with sub-milli-interface morphologies via direct ink writing for indoor formaldehyde removal. J Hazard Mater 427, 128190. https://doi.org/10.1016/j.jhazmat.2021.128190.
[58] Myers, A.L., 2002. Thermodynamics of adsorption in porous materials. AlChE J 48 (1), 145–160. https://doi.org/10.1002/aic.690480115.
[59] GB/T 18883-2022, 2022. Standards for indoor air quality. China Standard Press, Beijing.
[60] Chen, B., Jiang, Y., Tang, X., Pan, Y., Hu, S., 2017. Fully PAckaged Carbon Nanotube Supercapacitors by Direct Ink Writing on Flexible Substrates. ACS Appl Mater Interfaces 9 (34), 28433–28440. https://doi.org/10.1021/acsami.7b06804.
[61] Yang, G., Sun, Y., Limin, Q., Li, M., Ou, K., Fang, J., et al., 2021. Direct-ink-writing (DIW) 3D printing functional composite materials based on supra-molecular interaction. Compos Sci Technol 215, 109013. https://doi.org/10.1016/j.compscitech.2021.109013.
[62] Macedo, V.M., Pereira, N., Tubio, C.R., Martins, P., Lanceros-Mendez, S., Costa, C. M., 2022. 3D-printed carrageenan-based nanocomposites for sustainable resistive sensing devices. Polymer 262, 125456. https://doi.org/10.1016/j.polymer.2022.125456.
[63] Sas Brunser, S., Bargardi, F.L., Libanori, R., Kaufmann, N., Braun, H., Steinfeld, A., et al., 2023. Solar-driven redox splitting of CO2 using 3D-printed hierarchically channeled ceria structures. Adv Mater Interfaces 10 (30), 2300452. https://doi.org/10.1002/admi.202300452.
[64] Chen, Q., Chen, Z., Wang, Y., Tian, E., Mo, J., 2023. Hierarchical diffusion pathways into VOC adsorption films by direct ink writing and ammonium carbonate treatment. Chem Eng J 471, 144560. https://doi.org/10.1016/j.cej.2023.144560.
[65] In Seok, K., Ho Nam, C., 1982. The effect of turbulence promoters on mass transfer—numerical analysis and flow visualization. Int J Heat Mass Transf 25 (8), 1167–1181. https://doi.org/10.1016/0017-9310(82)90211-3.
[66] Kowalska, K., Barczak, M., Giannakoudakis, D.A., Bandosz, T.J., Borowski, P., 2023. Formaldehyde interactions with oxygen- and nitrogen-functionalized carbonaceous surfaces in the presence of moisture: computational approach vs experimental results. Carbon 215, 118443. https://doi.org/10.1016/j.carbon.2023.118443.
[67] Huang, P.-H., Hung, S.-C., Huang, M.-Y., 2014. Molecular dynamics investigations of liquid–vapor interaction and adsorption of formaldehyde, oxocarbons, and water in graphitic slit pores. Phys Chem Chem Phys 16 (29), 15289–15298. https://doi.org/10.1039/C4CP01922A.
[68] Boudot, M., Elettro, H., Grosso, D., 2016. Converting water adsorption and capillary condensation in usable forces with simple porous inorganic thin films. ACS Nano 10 (11), 10031–10040. https://doi.org/10.1021/acsnano.6b04648.
[69] Liu, J.C., Monson, P.A., 2005. Does water condense in carbon pores? Langmuir 21 (22), 10219–10225. https://doi.org/10.1021/la0508902.
[70] Pei, J., Zhang, J.S., 2011. On the performance and mechanisms of formaldehyde removal by chemi-sorbents. Chem Eng J 167 (1), 59–66. https://doi.org/10.1016/j.cej.2010.11.106.
[71] Suzin, Y., Buettner, L.C., LeDuc, C.A., 1999. Characterizing the ignition process of activated carbon. Carbon 37 (2), 335–346. https://doi.org/10.1016/S0008-6223(97)00138-3.